Remote Sens. **2014**, *6*, 6300-6323; doi:10.3390/rs6076300

OPEN ACCESS

remote sensing

ISSN 2072-4292

www.mdpi.com/journal/remotesensing

Article

Evaporative Fraction as an Indicator of Moisture Condition and Water Stress Status in Semi-Arid Rangeland Ecosystems

Francesco Nutini [1,*], Mirco Boschetti [1], Gabriele Candiani [1], Stefano Bocchi [2] and Pietro Alessandro Brivio [1]

[1] Institute of Electromagnetic Sensing of Environment, National Research Council of Italy (CNR-IREA), Via Bassini 15, Milan 20133, Italy; E-Mails: boschetti.m@irea.cnr.it (M.B.); candiani.g@irea.cnr.it (G.C.); brivio.pa@irea.cnr.it (P.A.B.)

[2] Department of Agricultural and Environmental Science, Universit à degli Studi di Milano, Milano 20133, Italy; E-Mail: stefano.bocchi@unimi.it

***** Author to whom correspondence should be addressed; E-Mail: nutini.f@irea.cnr.it; Tel.: +39-2-2369-9454.

Received: 14 April 2014; in revised form: 16 June 2014 / Accepted: 18 June 2014 / Published: 7 July 2014

Abstract: Rangeland monitoring services require the capability to investigate vegetation condition and to assess biomass production, especially in areas where local livelihood depends on rangeland status. Remote sensing solutions are strongly recommended, where the systematic acquisition of field data is not feasible and does not guarantee properly describing the spatio-temporal dynamics of wide areas. Recent research on semi-arid rangelands has focused its attention on the evaporative fraction (EF), a key factor to estimate evapotranspiration (ET) in the energy balance (EB) algorithm. EF is strongly linked to the vegetation water status, and works conducted on eddy covariance towers used this parameter to increase the performances of satellite-based biomass estimation. In this work, a method to estimate EF from MODIS products, originally developed for evapotranspiration estimation, is tested and evaluated. Results show that the EF estimation from low spatial resolution over wide semi-arid area is feasible. Estimated EF resulted in being well correlated to field ET measurements, and the spatial patterns of EF maps are in agreement with the well-known climatic and landscape Sahelian features. The preliminary test on rangeland biomass production shows that satellite-retrieved EF as a water availability factor significantly increased the capacity of a remote sensing operational product to detect the variability of the field biomass measurements.

Keywords: evaporative fraction; semi-arid rangeland; biomass estimation

1. Introduction

The ecosystem carrying capacity and food security of the West African Sahel relies on annual vegetation production, which is concentrated in a short rainy period of four months, on average, between July to October [1]. The majority of the Sahelian livelihood counts on these wet months to get by in the dry season. The management of existing natural resources by the local population has developed several strategies to cope with climatic difficulties, such as exploiting herd transhumance at the beginning of the dry season [2] or handling the seedling date in the beginning of the rainy period [3].

However, recurrent erratic rainfall or a drought period could affect Sahelian food security, as happened during the great drought of the past century [4] and recent local food crises [5]. Despite several adaptations of the Sahelian population to erratic climate conditions [6], food security still remains a concern, and an accurate estimation of regional yields plays an important role in food security [7].

The awareness of rangeland production in relation to water availability is of major interest for the implementation of operational monitoring systems to support policies aiming at reducing the socio-economic impacts of environmental stresses. As water availability is the main limiting factor for vegetation production, especially where average annual rainfall is lower than 500/600 mm [8,9], the interest to estimate rainfall and soil moisture at the regional scale in relation with biomass production has earned a lot of attention.

Several recent studies analyzed time series of rainfall and vegetation indices highlighting the Sahel as an area where vegetation production is rainfall driven and only locally influenced by human activities [9–13]. Other works in the area compared vegetation production to trends of soil moisture [14] and rain use efficiency [15], identifying water availability as the main driver of vegetation growth and dynamics in the Sahel. A shortwave infrared water stress index (SIWSI) has been proposed as an indicator of vegetation water stress [16], while a combination of thermal data and vegetation index [16] were used to produce qualitative maps of soil moisture along the Senegal River.

Compared to these methods, the estimation of evapotranspiration (ET) at the regional scale could give a more quantitative assessment of vegetation water status. ET is a key component of the water budget, and its estimation at different scales is of outmost importance for water management in agriculture [17] and food security programs [18]. ET can be appropriately measured at the field scale by lysimeters, scintillometers or eddy correlation techniques [18]. However, being highly dynamic in space and time because of complex interactions between soil, vegetation and climate [19], the quantification of its flux at the watershed scale is much more difficult than at a specific site [20].

Traditional methods to estimate ET assume homogeneous vegetation cover and structure, but these conditions are hard to meet for large regions [21]. For studies at regional and continental scales, monitoring models are coupled with remotely sensed data that can cope with the spatial and temporal variability of surface characteristics that affect evapotranspiration processes [18]. Several surface

characteristics, such as albedo, vegetation cover, leaf area index and land surface temperature, can be retrieved from satellite observations providing data for ET estimation from space.

Since the launch of Earth Observation satellites with thermal infrared channel, such as Landsat Thematic Mapper, NOAA-AVHRR and Terra/Aqua MODIS, several applications have been developed over near fully agricultural canopy covers and semiarid rangeland basins to estimate instantaneous ET and to scale up such estimations to daily ET.

One of the widely used methods [22] to estimate daily ET is based on the evaporative fraction (EF), which is defined as the ratio between latent heat flux and the total heat leaving the Earth's surface. A strong correlation between the value of EF at midday and the daytime average value has been observed [23,24], and it is often assumed as a constant daytime variable [18,21,25–32].

The EF has a strong link with soil moisture availability [33], which is the limiting factor of latent heat flux [29], and it is essentially controlled by water availability in the root zone [34]. The EF behavior at the landscape scale is correlated to the amount of vegetation cover [35], the timing of rainfall events [36], the successions of wet and dry periods [37], the vapor pressure deficit and vegetation photosynthesis activity [38].

EF has an annual behavior related to rainfall events, with peaks during the rainy season and decreasing when soil is drying [39]. In fact, a work conducted over paddy rice area shows that EF always has values close to one, because soil moisture was almost saturated [38].

Recent works conducted in correspondence with eddy covariance stations in North America [39], the northern Australia savannah [40] and the Sahelian region [41] proposed the EF as an indicator of water stress to correct vegetation production estimation. The results of these studies indicated that the use of field-measured EF values within a light use efficiency (LUE) model allows one to improve the estimate of biomass production.

EF can be derived from satellite data using the NDVI-temperature triangle method [42] or the simplified surface energy balance index (S-SEBI) model [43], following the relationship between albedo and land surface temperature [18]. This last approach found applications with a wide range of remotely sensed data and in different ecosystems.

The accuracy of EF estimated by S-SEBI was demonstrated in comparison with other approaches, both for high resolution ASTER images [44] and low resolution NOAA-imagery [18]. Daily ET values, estimated via the EF approach, were validated at the field scale with flux measurements on cropland [27], as well as at the regional scale over the Iberian Peninsula with Digital Airborne Imaging Spectrometer (DAIS) high resolution data [26].

Outside of Europe, the use of this approach has been reported in the Mediterranean landscapes of Chile [45] and in the cotton crops of Brazil [46], demonstrating the suitability of the method in semi-arid areas.

The aim of this work is to retrieve EF from satellite data in the Sahelian rangeland ecosystem and to evaluate the parameter as a moisture indicator, useful also as a correcting factor in the radiation use efficiency biomass estimation model.

The application of the S-SEBI method requires the presence of wet and very dry surfaces [26,43,47]; these conditions are well satisfied over the West Africa area, thanks to presence of the Sahara Desert and stable, humid ecosystems, such as the Niger Inner Delta and Lake Chad. In particular, the goals of this research are: (i) to set-up an automatic procedure to derive EF maps

from MODIS products; (ii) to evaluate EF estimation using *in situ* data and to assess EF maps at the regional scale; and (iii) to evaluate the improvement brought by satellite-retrieved EF to the accuracy of the biomass production model.

2. Study Area

The study area covers 1200 × 2400 km over Niger and Chad. The northern part includes the Sahara Desert, where less than 200 mm of rain falls every year and human presence is almost absent (Figure 1). The central part is located on the Sahelian belt, identified by the isohyets of 200 and 600 mm. This zone is mainly characterized by semi-arid savannah, where pastoralism is the most important livelihood activity, with localized evidence of agricultural activity (<20% of cultivated areas; [48]). The southern part of study area belongs to the Sudanian savannah, characterized by wetter climate (annual rain greater than 600 mm), an intensive farming system and less dependency on rain for vegetation productivity [4,10]. The rainy season of the whole study area is essentially from July to October and slightly longer in southern areas, with almost zero precipitation during the rest of the year.

A number of humanitarian crises have hit this area over recent years; although several are from concurring causes, such as food supply, livestock management, environmental degradation and household coping capabilities, low or erratic rainfall remains the key factor triggering the crisis [4,5,49]. In this region, the population has increased during the past 25 years [50]. The rural population is still growing, contrary to many other parts of the world, leading to heavy pressure on the environment, especially during adverse years.

Figure 1. The study area overlaid on the regional GlobCover (GC) map of Africa [51]; the red star shows the position of the eddy covariance station; the red diamonds represent the field sites; the blue lines indicate the isohyet boundaries of 200–600 mm/year.

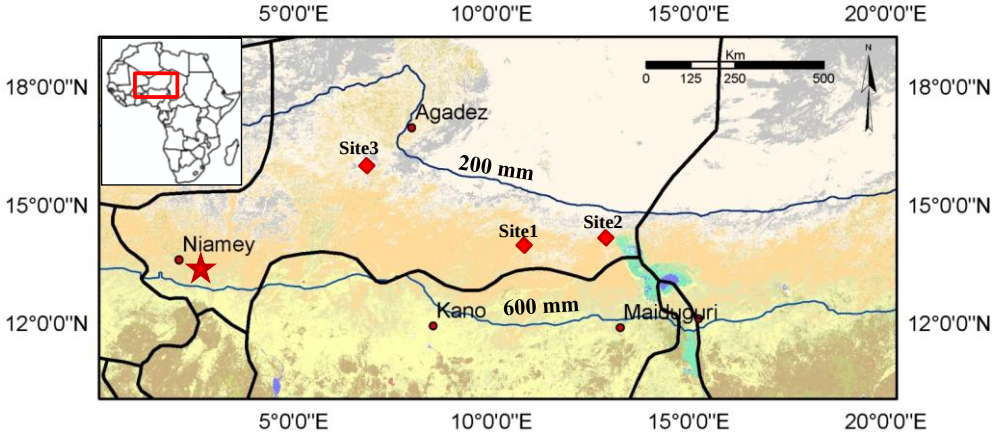

3. Materials

3.1. Earth Observation Data

According to the S-SEBI approach [43], the retrieval of EF from satellite data is based on the relationship between albedo and land surface temperature (LST). Two MODIS products were then considered: MCD43B3, *i.e.*, the hemispherical reflectance (black-sky albedo) 8 days at 1-km spatial

resolution, and MOD11A2, *i.e.*, land surface temperature 8 days at 1-km spatial resolution [52]. In order to cover the entire area of interest, two MODIS tiles (h18v07, h19v07) were downloaded for 10 years (2000–2009), summing up to about 450 images per tile.

Other satellite-derived products were used for analysis and evaluation purposes. For the analysis of the EF contribution to biomass production, we used dry matter productivity (DMP) maps [53]. DMP is a satellite-derived product, developed at the Flemish Institute for Technological Research (VITO), that quantifies the daily increase of dry biomass (growth rate) and is expressed as kilograms of dry matter (kg·DM) per hectare per day. The DMP product used in this exercise is a 10-day composite at 1-km spatial resolution covering the period 2000–2009.

Ancillary satellite data consist of rainfall and vegetation maps for the study area. Rainfall estimation (RFE 2.0) is provided by Famine Early Warning Systems Network (FEWS) every 10 days at 8-km spatial resolution [54]. RFE 2.0 is produced by a combination of Meteosat 5 data (satellite infrared data) and daily rain gauge data extracted from the WMO's Global Telecommunication System (GTS) with the additional integration of the two new Special Sensor Microwave/Imager (SSM/I) instruments on-board the Defense Meteorological Satellite Program satellites and the Advanced Microwave Sounding Unit (AMSU). Vegetation maps are represented by Normalized Difference Vegetation Index (NDVI) provided by the SPOT-Vegetation satellite (VGT) sensor every 10-days at 1-km spatial resolution [55]. Finally for the analysis of EF behavior for different vegetation types, the regional GlobCover (GC) map for Africa with 300-m spatial resolution was used [51], which describes land cover classes over the entire study area.

3.2. Field Biomass and Flux Measurements

Field biomass data have been provided by Action Against Hunger (ACF) for three different sites in Niger (Figure 1). Three site were analyzed: the first site is located in a tiger bush area 35 km north of Nigeria border (Site 1, Longitude 10.9, Latitude 13.7); the eastern site is located around Lake Chad (Site 2, Longitude 12.8, Latitude 13.95), while the northern site (Site 3, Longitude 6.8, Latitude 15.8) is located around Agadez, which is the upper limit of pasture activities [56,57]. Biomass measurements were collected following the quick double-sampling technique [58] to calibrate/validate ACF satellite maps of available forage [59]. Overall, 19 annual biomass values/data are available for the period of 2000–2009 (Table 1). These ground samples provide crucial information for the evaluation of EF capability as a water stress factor in biomass estimation.

Table 1. Field data cardinality and average sampled values of the three field biomass measurements.

Site	#Data	Period	AVG (kg/ha)	Max (kg/ha)	Min (kg/ha)	Stand Deviation (kg/ha)
Site 1	6	2003; 2005–2009	963	1,463	342	508
Site 2	8	2000; 2002–2009	371	1,047	0	378
Site 3	5	2001; 2005; 2007–2009	888	1712	326	614

Flux measurements were collected at an eddy covariance tower situated in the Wankama catchment (Figure 1), 60 km east of Niamey, Niger. This site presents the typical Sahelian landscape with sparse savannah and millet fields. Daily data of net radiation ($W \cdot m^{-1}$) was measured every minute by the

tower instruments at a height of 2.5 m; these data are supplied to the user from the CarboAfrica project through FLUXNET measurement network as the average over 30-min periods [60]. This variable is available as a Level 2 product, *i.e.*, not gap-filled, but checked/filtered for out-of-range values or clearly wrong data [60]. The daily latent heat flux data ($W \cdot m^{-1}$), processed with despiking, double rotation and gap filling following the indications of [61], were obtained from the publication of [62]. Both fluxes are available for the period between June 2005 and June 2007, including the wet season of 2005 and 2006.

4. Method

4.1. Estimation of Evaporative Fraction

The more widely applied method for ET estimation with passive remote sensing is the energy balance equation [18]. The land surface energy balance is the thermo-dynamic equilibrium between turbulent transport processes in the atmosphere and laminar processes in the sub-surface [17]. The basic formulation can be written as:

$$R_n = \lambda E + G_0 + H \quad (1)$$

where *Rn* is the net radiation, λE is the latent heat flux (λ is the latent heat of vaporization of water and E is evapotranspiration), G_0 is the soil heat flux and *H* is the sensible heat flux.

Evaporation and transpiration occur simultaneously, and there is no easy way of distinguishing between the two processes: when the crop is small, water is predominately lost by soil evaporation, but once the vegetation completely covers the soil, leaf transpiration becomes the main process [28]. Many satellite-based approaches estimate daily ET, exploiting the *EF* factor [26,32,44], defined as the ratio between the latent heat flux (λE) and the available energy at the land surface ($R_n - G_0$):

$$EF = \frac{\lambda E}{R_n - G_0} \quad (2)$$

In the present work, the *EF* estimation is obtained using the albedo-temperature method [43]. This approach allows one to compute the *EF* for every pixel as the relative distance from two lines, called the dry edge and wet edge, defined through a date-specific albedo-LST relationship (Figure 2). The method's accuracy is dependent on the presence of humid and arid surfaces in the study area.

Figure 3 provides the flow chart of the steps followed for the EF estimation from satellite products, for each available date of satellite products. Albedo and LST data were extracted from the digital numbers (DN) of MCD43B3 (layer 10) and MOD11A2 (layer 1), as indicated by the MODIS product description [52], while information on LST data quality as derived from Layer 2 of the MOD11A2.

Before starting the *EF* calculation, pixels flagged as "no-data" or "low quality" were masked out and excluded from the analysis.

To perform the *EF* estimation, the albedo-LST scatterplot is derived for a single date (Figure 2) and analyzed to extract minimum and maximum temperature values for all of the albedo classes identified from statistical analysis [63].

Figure 2. Scatterplot between surface albedo and LST. Blue circles correspond to minimum temperature values for each albedo class, which are used to compute the wet edge (lower limit of the graph) through linear regression. Red circles correspond to the maximum temperature values for each albedo class, which are used to compute the dry edge (upper limit) through linear regression. T_H (maximum temperature) and $T_{\lambda E}$ (minimum temperature) represent the values used in the calculation of the EF for the pixel *i*.

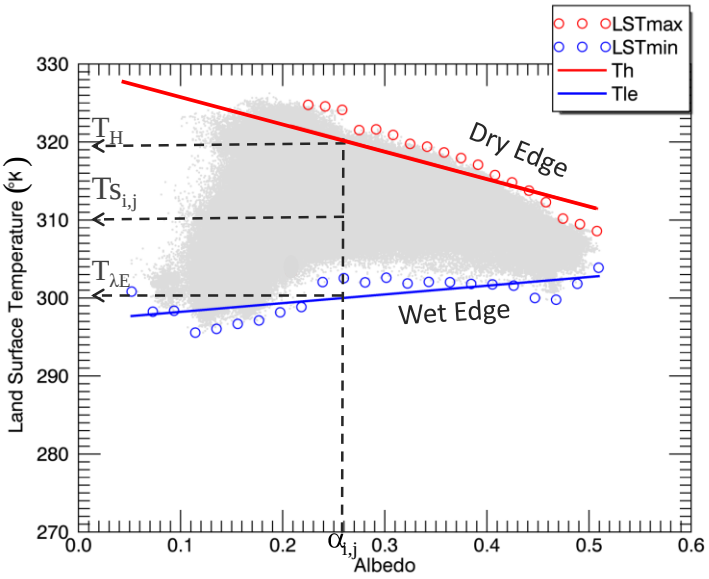

Figure 3. Flowchart for the evaporative fraction estimation from the MODIS products of albedo and land surface temperature.

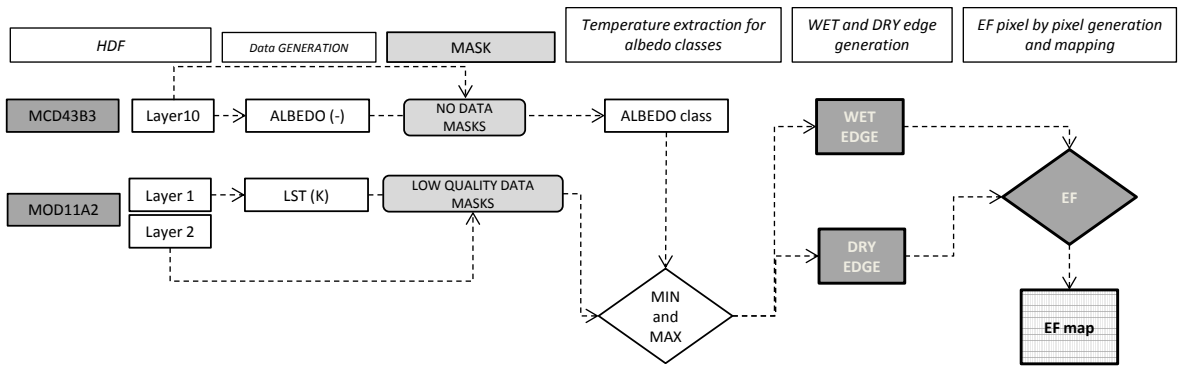

The series of maximum and minimum LST values are used to calculate the date-specific dry and wet edge equation through linear regression:

$$dry\ edge: T_H = m_{dry}\,\alpha_0 + q_{dry} \quad (3)$$

$$wet\ edge: T_{\lambda E} = m_{wet}\,\alpha_0 + q_{wet} \quad (4)$$

where *m* and *q* represent the parameters (slope and intercept) of the two regression lines, α_0 represents the albedo, while T is the land surface temperature.

The dry edge was defined considering only pixels in the radiative controlled condition, commonly identified as the maximum temperature data for all of the albedo values greater than the inflection

point of the concave temperature-albedo scatterplot [17]. This condition was empirically defined for an albedo value above 0.2, as used also by [44].

Exploiting the dry and wet edge, the EF can be calculated for every pixels *i*, dividing the difference between T_H and the temperature pixel T_S by the difference between T_H and $T_{\lambda E}$:

$$EF_i = \frac{T_{H\,i} - T_{s\,i}}{T_{H\,i} - T_{\lambda E\,i}} \quad (5)$$

where T_{si} is the temperature value of the pixel i and T_{Hi} and $T_{\lambda Ei}$ are respectively the maximum and minimum temperature value derived by the dry and wet edge functions for a given albedo value α_i.

The *EF* equation can be rewritten as:

$$EF_i = \frac{\left(m_{dry}\,\alpha_i + q_{dry}\right) - T_{S\,i}}{\left(m_{dry}\,\alpha_i + q_{dry}\right) - \left(m_{wet}\,\alpha_i + q_{wet}\right)} \quad (6)$$

this procedure, implemented with an *ad hoc* code in IDL language (Interactive Data Language, version 8.2), was applied to each pixel of the image and on each date available for both MODIS tiles h18v07 and h19v07.

The maps estimated at the same dates were mosaicked, obtaining EF maps of 122 × 2400 km to cover the entire study area.

4.2. Evaluation of the Estimated EF

Since it is well known that *EF* is related to water availability provided by rainfall, particularly in the natural vegetation of semi-arid environments, vegetation growth and land cover [29,35,38,64], we used the RFE, SPOT-VGT NDVI and GlobCover classes to assess the consistency of EF estimation. In particular, average and relative standard deviation (RSD) maps of EF are computed from the 448 8-day EF maps and analyzed for the major land cover classes of the study area, thanks to GlobCover map. This analysis was conducted in order to evaluate the coherence between the EF and the expected behavior over different vegetation covers.

In correspondence with the eddy covariance tower, EF behavior was compared to rainfall events and vegetation growth.

Quantitative evaluation of the reliability of EF estimations as a moisture (water stress) indicator is accomplished using the eddy covariance data from Wankama station.

Due to the different time steps of satellite estimation and flux measurements, the satellite-derived EF was compared with the 8-day average of daily ET corresponding to the MODIS composite. Data from the tower measurements identified as outliers from statistical analysis and EF satellite estimation flagged as low quality were excluded by the analysis. Moreover, thanks to Equation (7), it was possible to compare *in situ* estimation of EF with satellite-derived *EF*:

$$EF_{eddy} = \lambda E_d / R_{n\,d} \quad (7)$$

where Rn_d and λE_d are the daily net radiation and the daily latent heat flux, respectively.

4.3. Biomass Estimation

The seasonal cumulative DMP is an indicator of the annual rangeland production [15,65–67], which can be compared to the ground data, that represents the total annual herbaceous production measured in field.

In order to compare satellite data with field samples, EF and DMP were extracted in correspondence with the field sites location in a buffer of 1 km. The 10-day DMP product for the period of July to October, referred to here as JASO, was cumulated to obtain the annual syntheses of dry matter production (DMP^{JASO}).

The EF was exploited as a water availability factor to correct the satellite estimation of vegetation biomass (DMP).

DMP and EF have different time steps (10 and 8 days, respectively); consequently, monthly values were calculated in order to use the water availability/stress factor in the biomass estimation model.

For *EF*, the monthly average ($\overline{EF}^m$) was computed for every month (m) and every site (s):

$$\overline{EF}_s^m = \frac{\sum_{t=1}^{n} EF_{s,t}^{8D}}{n} \quad (8)$$

where EF^{8D} is the estimated water stress from Equation (6), s is the site and n is the cardinality of the 8-day *EF* data for each month.

For *DMP*, the monthly sum (DMP^m) was calculated to represent the total dry biomass produced during every month at each site:

$$DMP_s^m = \sum_{t=1}^{3} DMP_{s,t}^{10D} \quad (9)$$

where DMP^{10D} is the 10-day biomass estimation product, t is the number of DMP data within the month and s is the site.

Monthly $\overline{EF}^m$ and DMP^m values were than integrated and annually cumulated by the following equation for each site:

$$DMP_s^{JASO*} = \sum_{m=1}^{4} DMP_s^m \cdot \overline{EF}_s^m \quad (10)$$

where EF^m and DMP^m are the variable obtained from Equations (8) and (9), s is the site and 4 is the number of months in the JASO period.

Finally, to quantify the improvement of DMP^{JASO}*, the comparison between observed and estimated values were performed and difference-based statistics [68] together with regression analysis and Akaike information criterion (AIC) [69], Equation (11), were conducted.

$$AIC = n \cdot \log(MSE) + 2 \cdot T \quad (11)$$

where n is the number observed/simulated pairs, *MSE* is the mean square error and T is the number of inputs in the model.

AIC with a lower value indicates whether the increase in the input of a model is compensated for by a significant increase in accuracy.

5. Results and Discussion

5.1. Dry and Wet Edge Statistics

Figure 4 shows the average intercepts (a) and slopes (b) for the calculated dry (empty triangles) and wet (filled circles) edge. Every point represents the average of 10 estimations from 2000 to 2009 together with a bar representing the standard deviation. The dry edge statistics of the slope and intercept are on the second y-axis, to facilitate a comparison with the wet edge statistics. The gray shaded area displays the period when generally no rainfall occurs in the study area.

Figure 4. Eight-day average values of the intercept (**a**) and slope (**b**) obtained from dry and wet edge lines for the 2000–2009 period. Shaded gray areas represent the dry season. Plots show three albedo-LST scatterplots for the year, 2009.

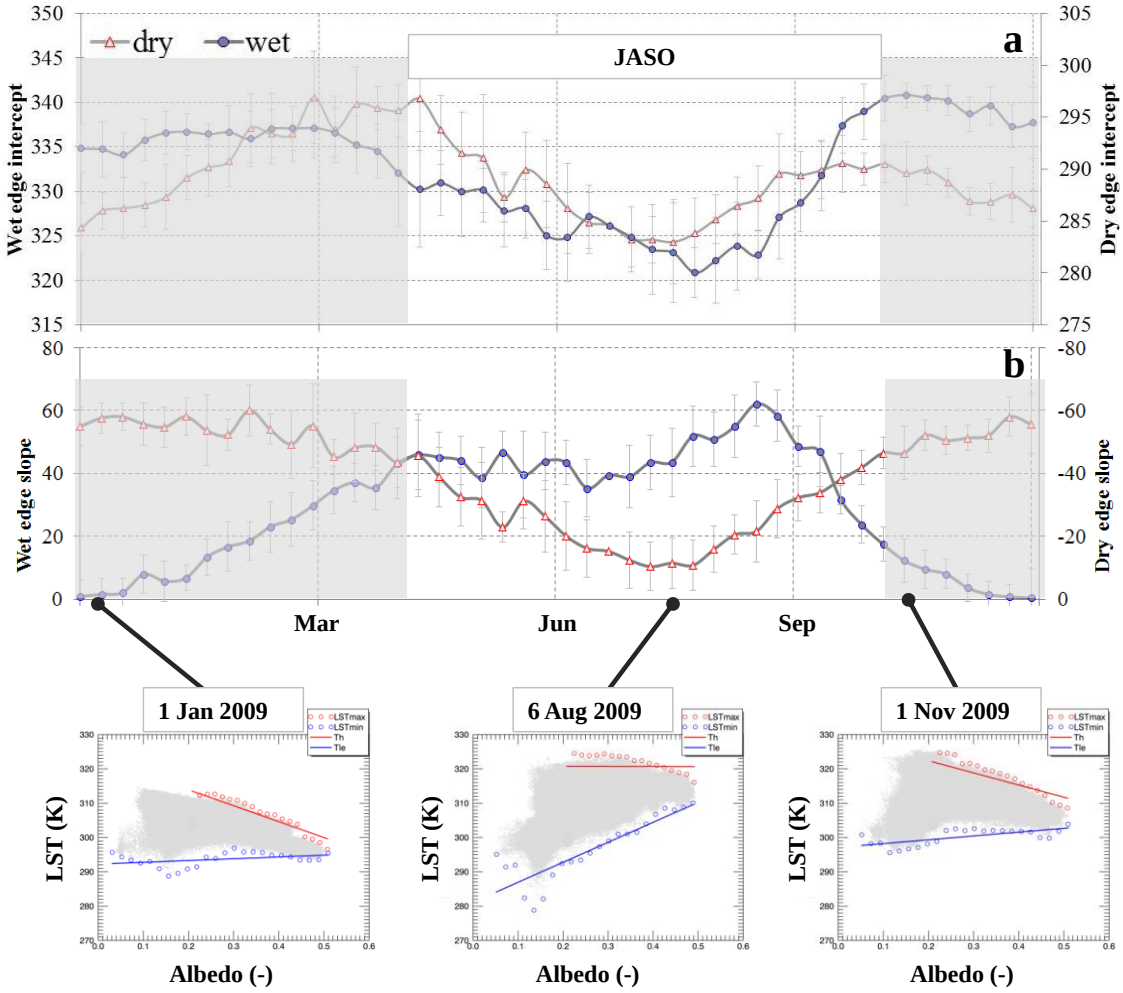

The intercept of the dry edge follows the typical behavior of West African temperature [70], with lower values during the wet season (June–October) and two peaks during the dry season, the former in April and the latter in November.

The Wet edge intercept has lower value in the wet season and stable, higher values during the dry one. The average slope coefficient shows that during the dry season, the wet edge is generally

horizontal (values close to zero), while the dry edge has a high negative slope (values down to −60), as shown by a similar analysis conducted in the Mekong Delta [71].

On the contrary, in the rainy period, the dry edge is almost flat, while the wet edge has a strong positive slope (values up to 60). In general, the coefficients of wet and dry edge follow a seasonal behavior driven by rainfall and incoming solar radiation.

Figure 4 shows also three examples of the albedo-LST scatterplots. The first displays the dry season condition with the flat wet edge and the second one the wet condition with the flat dry edge. The last scatterplot displays an intermediate condition at the end of the rainy season, when the two lines are both oblique and the maximum LST is higher.

The maximum albedo value of 0.6 in the scatterplots highlights the presence of high reflective surfaces [72], which correspond to brighter desert areas. These areas are stable through the season; hence, they are present in every plot.

The areas with lower temperature (below 305 K) and lower albedo (below 0.2) correspond to a permanent humid zone, such as the Lake Chad area and the border of the Niger River.

The permanent presence through the years of these two extreme situations allows one to produce a meaningful scatterplot describing the contrast between dry and wet areas, hence guaranteeing the conditions for the application of the method [17,43].

5.2. Evaluation of EF Spatial Patterns

Figure 5 shows the mean EF map obtained from the estimated 448 maps for the period of 2000–2009 (a), together with the RSD (b). As expected, the mean values vary between zero and one, where zero indicates the hyper-arid condition and one the humid area. The areas with a mean rainfall below 200 mm, belonging to the Sahara Desert, were excluded from the analysis, since these areas are not populated and EF estimation makes sense and is useful only on partially vegetated surfaces. Permanent arid areas ($EF < 0.2$) can be found close to the desert, especially in the Agadez province (Niger) and in the central part of Chad. Both of these areas rely on the "high-risk Sahel's vulnerable zone", where the main livelihood activity is transhumant herding [73].

The hyper-humid area ($EF > 0.7$) can be found in correspondence with permanent water bodies, such as Lake Chad [74], Lake Fitri (central Chad) and Lake Kainji (west Nigeria). Furthermore, the woody hills in Nigeria, characterized by a high level of rainfall (more than 1200 mm/year), are generally well humid. The Sahelian belt is characterized by medium-low average values of *EF* (below 0.5) apart from the river belts: Niger in the west part of study area, Yobe along the Niger-Nigeria border and Chari south of Lake Chad.

The RSD (Figure 5b) is a normalized measure of EF data dispersion. The equation of the RSD is obtained dividing the standard deviation by the mean. The lower percentage indicates a lower variability in the EF time series.

The map highlights areas in red and orange with stable *EF* (RSD < 30%) from 2000–2009. These areas belong to lakes, rivers and wet regions in central Nigeria, which are also the regions characterized by high *EF* average values (Figure 5a). Hence, these well-watered areas have maintained their condition across the years analyzed.

Figure 5. The map of the average EF (**a**) and relative standard deviation (**b**) derived from 448 EF eight-day maps (2000–2009). Isohyets were calculated from rainfall estimation (RFE) data for the same period. The hyper-arid areas (<200 mm·year^{-1}) are masked out, and the GlobCover map is in the background.

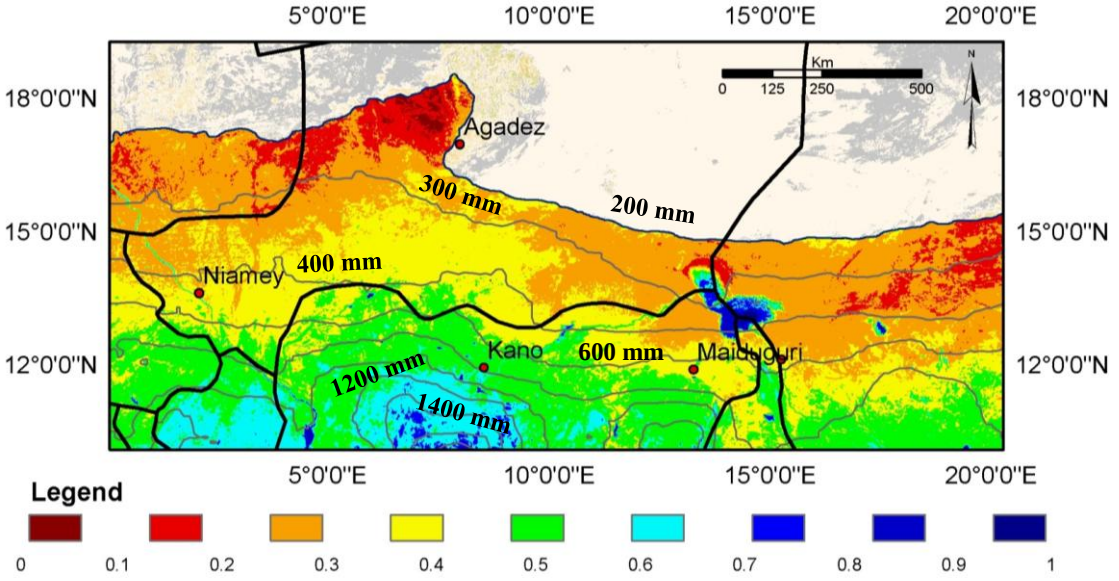

(**a**)

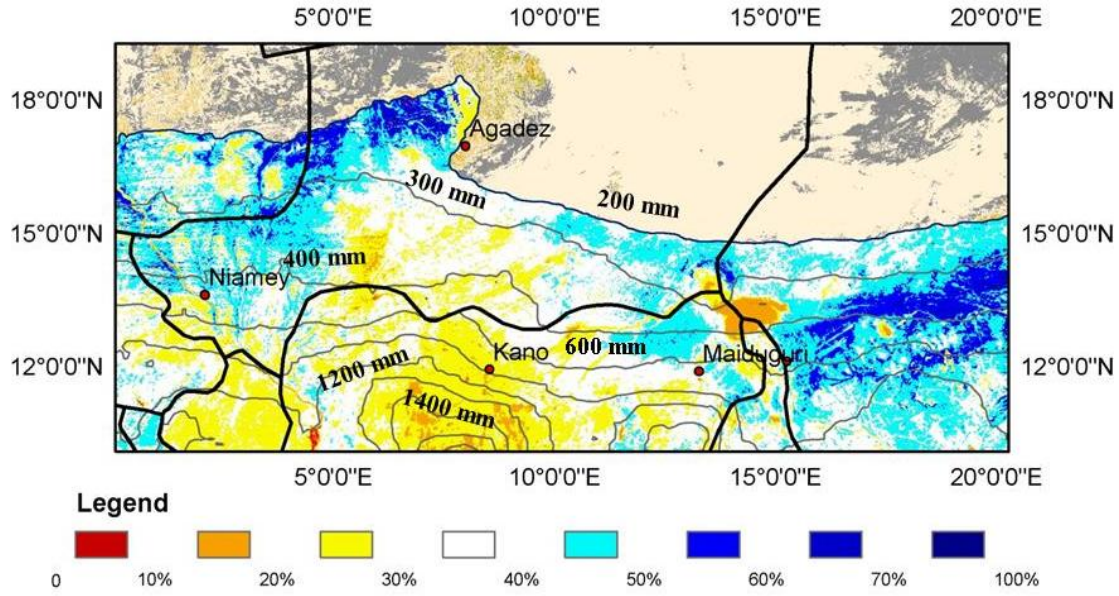

(**b**)

Vice versa, higher variation in EF values (RSD > 50%, blue and light blue) can be found in the northern Sahel (northern-western Niger and central Chad). In particular, in western Niger, the fossil valleys display a stronger variability of EF data compared to the surrounded rangelands, because of the greater water availability thanks to the morphopedological characteristics, as observed in [75]. The high RDS indicates that the EF data of these areas can vary abruptly, thanks to the strong seasonality (intra-annual variability).

The high EF variability of northern areas in Niger, characterized by the small EF average, can be driven by particularly favorable years (inter-annual variability).

The average EF map has been analyzed by GC classes (Figure 6). The GC classes are sorted from the mainly northern classes (GC_200) to the southern (GC_130), except for the classes of wetland (GC_180) and water body (GC_210). The most common classes are the bare areas (GC_200) and grassland savannah (GC_140). These two classes cover 70% of the entire study area.

Figure 6. Percentage of GC classes over the study area (codes and map color are reported) and the statistics of EF data for each LC classes (average (AVG) and relative standard deviation (RSD)). Red and green indicate land cover with a lower of a higher EF average, respectively.

LC (GC)				EF [-]	
Code_1	*Code*	*Description*	*%*	*AVG*	*RSD(%)*
200	200	Bare areas	16%	0.38	21.91
	201	Consolidated bare areas (hardpans, gravels, bare rock, stones, boulders)	12%	0.39	21.32
	202	Non-consolidated bare areas (sandy desert)	23%	0.51	17.57
140	140	Closed to open (>15%) herbaceous vegetation (grassland, savannas or lichens/mosses)	11%	0.36	18.01
	144	Closed (>40%) grassland	7%	0.42	16.32
110	110	Mosaic forest or shrubland (50-70%) / grassland (20-50%)	3%	0.44	22.92
30	30	Mosaic vegetation (grassland/shrubland/forest) (50-70%) / cropland (20-50%)	7%	0.46	17.12
20	20	Mosaic cropland (50-70%) / vegetation (grassland/shrubland/forest) (20-50%)	4%	0.53	16.59
10	10	Irrigated croplands	10%	0.60	13.33
60	60	Open (15-40%) broadleaved deciduous forest/woodland (>5m)	0%	0.64	8.39
130	130	Closed to open (>15%) (broadleaved or needleleaved, evergreen or deciduous) shrubland (<5m)	7%	0.58	11.99
180	180	Closed to open (>15%) grassland or woody vegetation on regularly flooded or waterlogged soil - Fresh, brackish or saline water	1%	0.67	18.40
210	210	Water bodies	0%	0.83	11.97

On average, the GC class with the highest EF value (EF = 0.83) is water bodies (GC_210). Among the vegetation classes, only irrigated crops (GC_10), forest (GC_60) and wetland have a mean EF greater than 0.6. The most arid classes (GC_140 and GC_200), with a mean EF lower than 0.4, describe the typical landscape of the northern Sahel [50].

This analysis shows that the spatial patterns of EF data (long-term average) are in agreement with the well-known climatic and landscape features of these areas. A similar analysis conducted in China [21], Europe [26] and Africa [22] demonstrated that EF maps build up spatial and temporal patterns coherent with the presence of different vegetated surfaces, different climatic conditions and different seasonal behavior of vegetation.

5.3. Comparison of Seasonal EF Estimations with Eddy Covariance Data

5.3.1. Temporal Dynamics of the Variables

Figure 7 presents the time series of net radiation, ET and EF measured at the Wankama eddy covariance tower (black lines) and the satellite-derived time series of EF (red dashes), RFE (blue bars),

NDVI (green line), albedo (cyan line) and LST (gold line) extracted by the corresponding image pixel for the years 2005 (Figure 7a) and 2006 (Figure 7b). The Wankama eddy tower, placed in millet fields, is characterized by the typical Sahelian behavior of rainfall and vegetation growth [62].

Figure 7. From top to bottom, the temporal behavior of daily net radiation; daily evapotranspiration; EF-derived from the eddy covariance tower data at the Wankama site (black lines) together with eight-day EF estimation from MODIS data (red dashes); decadal NDVI-VGT (green line); decadal precipitation (blue bars), eight-day MODIS albedo (gray line) and eight-day MODIS temperature (yellow line) for 2005 (**a**) and 2006 (**b**). Vertical lines represent the start and finish of the JASO period, doy the Day Of the Year.

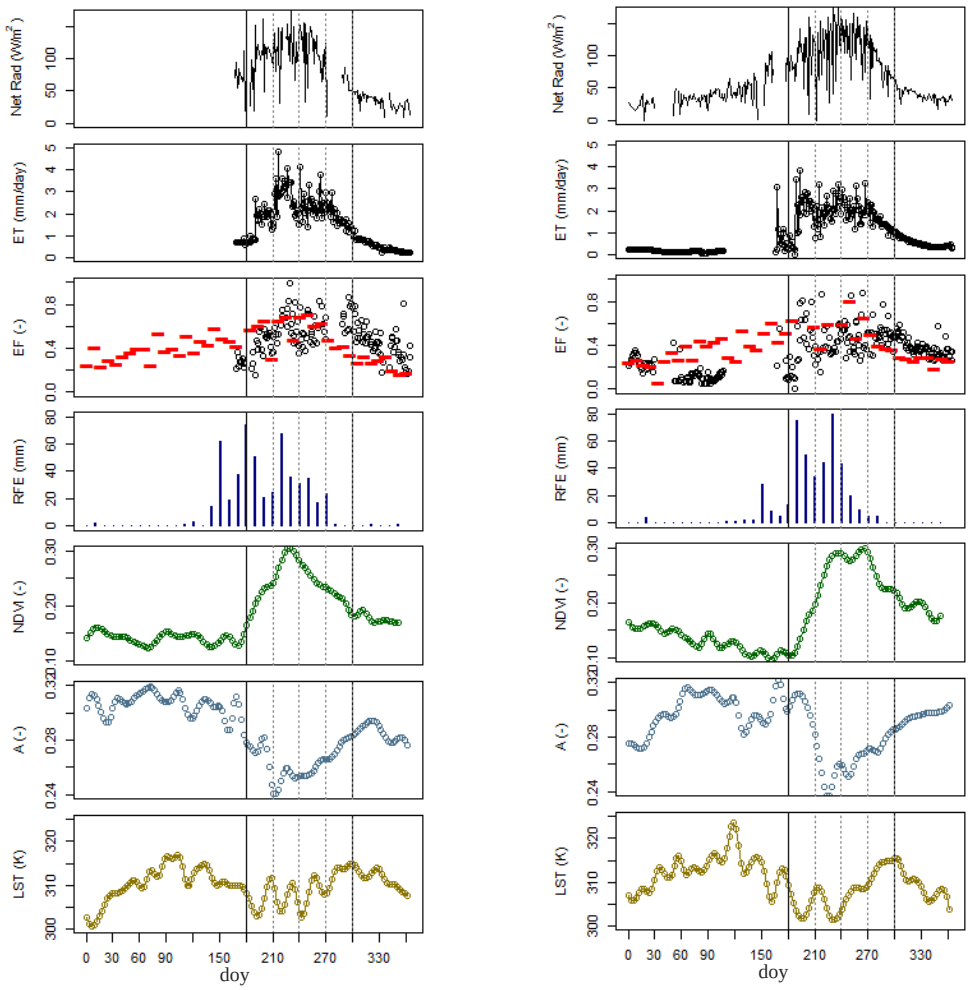

Vertical black lines indicate the average Sahelian wet season as being from July to October (JASO). The zero value of the satellite EF estimation, due to cloud contamination or other atmospheric interference in the data, was masked out from this analysis.

Figure 7a shows the time series of remote sensed and measured variables for the year, 2005. The first eddy measurement was recorded in June (doy 160), after the beginning of rain. ET shows the peak (>4 mm/day) in August, as well as net radiation. RFE shows an early start of the rainy season

compared to the JASO, with an intense rainfall period of 60 mm in May (doy 155). In total, 524 mm fell in 2005.

The red dashes indicate the eight-day period of satellite EF estimation from Equation (6) together with the *in situ* calculated EF from Equation (7). Both of the EF time series show higher values in the rainy season and drops in correspondence with the low ET value (e.g., doy 210 and 240). MODIS-derived EF decreases smoothly after doy 270, as happens for ET.

The vegetation behavior, highlighted by NDVI, shows the start of the season around doy 200 (19 July), about 50 days after the start of rainfall, because of the necessary time for germination [75]. NDVI has a specular behavior compared to albedo, as expected from the progressive cover of bare soil due to vegetation growth. The last two time series in Figure 7a display albedo and LST data. Both show a high value during the dry season, indicating a warm and bare surface. The rainy season has an average LST of 308 K (~35 °C), lower than the dry season average (311 K), because incoming energy during is exploited by evaporative and transpirative processes.

Figure 7b shows the same variables for 2006. The rainy period is shorter and less abundant compared to the previous one, with 430 mm of total rainfall. The estimated EF reaches a peak of 0.8 at doy 240 (28 August). The main EF drop is visible (doy 210) in correspondence with the drier period of the wet season, between the two main rain events. Both EF and ET rapidly decrease their values at the end of the wet season (doy 270). Higher vegetation growth occurs between August and September, and NDVI shows the presence of vegetation also in November–December (doy 300–360, NDVI ~0.2), even if EF and ET show that the area is completely dry.

The temporal behaviors of field measurements and satellite-derived data for 2005 and 2006 display high variability between dry and wet months. The 2005 wet season had an early start, while 2006 had a very late start, as well as an earlier end. Hence, the two years had different seasonality in terms of rainfall amount and distribution [62]. Among the several satellite-derived variables, estimated EF shows a higher correlation with estimated rainfall (data not shown), as expected from previous field studies [36,37,64,70], and in general, the estimated EF looks to be in accordance with the ET behavior and eddy covariance-derived EF. The temporal behavior of the EF variable is more noisy compared to the time series of other satellite-derived variables and hardly zero also in the absence of rainfall [39], as also displayed by eddy-derived EF.

Both MODIS estimation and eddy EF have comparable values during the wet season (JASO), showing a higher average value for the wetter year, 2005 ($\mu = 0.45$; $\sigma = 0.07$ for satellite and $\mu = 0.51$; $\sigma = 0.13$ for *in situ*, respectively), when compared to the drier 2006 ($\mu = 0.39$; $\sigma = 0.07$ and $\mu = 0.34$; $\sigma = 0.09$ for the satellite and *in situ*, respectively).

5.3.2. Correlation Analysis with ET

In order to evaluate the reliability of EF as a moisture indicator, a correlation analysis has been conducted between satellite *EF* estimation (y-axis) and ET measured by the eddy covariance tower (x-axis) (Figure 8).

The EF resulted in being significantly correlated to ET ($p < 0.001$), with a regressive coefficient of 0.54 pooling together the two years (2005–2006). ANCOVA analysis reveals that single year correlations (2005, $r^2 = 0.62$; 2006, $r^2 = 0.45$) were not significantly different ($p < 0.05$).

This correlation is biased by estimated EF in the late, dry season (January–May), when no rain and no vegetation are present, confirming that EF is noisy in the dry season [39].

Figure 8. Correlation between estimated EF (y-axis) and measured ET (x-axis) for both years 2005 (gray) and 2006 (purple) (n = 57).

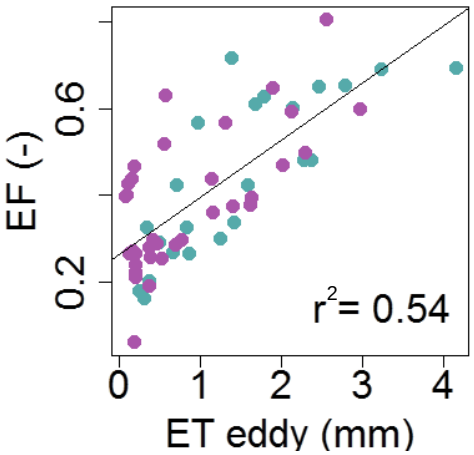

As expected the measured net radiation is better correlated with ET (r^2 = 0.64), since it represents the climatic driving force of evaporative and transpirative processes. In order to investigate if *EF* can improve the capability to explain the variance of ET, a multiple regression was performed between ET as a dependent variable and two independent variables, the measured Rn and the simulated *EF*.

Result shows that both the explanatory variables significantly contribute to the explanation of ET variability (70% of the total variance). Rn resulted in being more important, explaining about 64% of the total variance (p < 0.001), and *EF* significantly improved the model with a further 6% of variance explanation (p < 0.01). These results indicate that *EF* estimated with low resolution satellite data is well correlated with the field measured flux and gives a statistically significant contribution to the explanation of ET variability. It is important to remember that the *EF* data is derived by 1-km albedo and LST products; this aspect can strongly limit the comparison with field data acquired on small plots in a heterogeneous environment.

5.3.3. Biomass Estimation Improvements Using *EF* Correction

The results of previous analysis confirmed the validity of *EF* as a moisture indicator supporting the idea of using this satellite estimation as a water stress factor in a radiation use efficiency model. Previous studies, exploiting only field-based *EF*, demonstrated that *EF* can be exploited as a water stress efficiency factor [41].

To assess this contribution, the performance of operational products (DMP^{JASO}) and biomass estimation corrected by *EF* (DMP^{JASO}*) were compared with available annual production data over three test sites in Niger.

In Figure 9a are shown the three sites' specific correlations between the available field data and DMP^{JASO}. The three sites show different correlations: in particular, Site 1 (black dots) presents little correlation (r^2 = 0.49, intercept = 1300, slope = 0.3); Site 2 (blue squares) shows an average correlation (r^2 = 0.51, intercept = 700, slope = 1.1); and Site 3 (red triangles) has a high correlation (r^2 = 0.66,

intercept = 400, slope = 0.3). All three sites have the typical Sahelian biomass production [76], ranging from 100 (kg ha^{-1}), in adverse years, to 20-times higher production in favorable climatic conditions.

Figure 9. The correlation between annual biomass samples and satellite estimation DMP^{JASO} (DMP, dry matter productivity) (**a**), DMP^{JASO}* (**b**) and normalized data (**c**) (n = 19). Black dots for Site 1, blue squares for Site 2 and red triangles for Site 3. Black and gray diamonds represent normalized DMP^{JASO} and DMP^{JASO}, respectively. The dotted line indicates the 1:1 line.

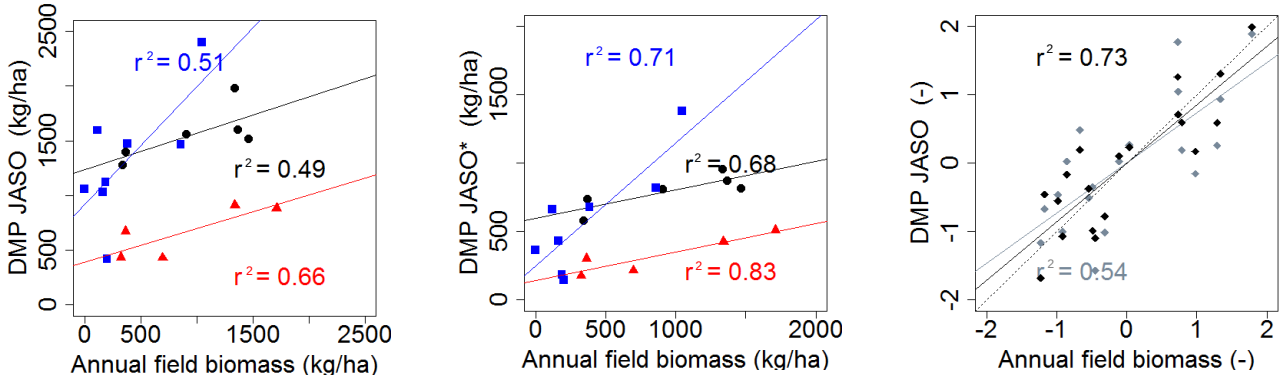

(**a**) (**b**) (**c**)

Results demonstrate that the DMP^{JASO} is able to detect the field biomass variability with site-specific, good correlation; however, the analysis of intercept and slope variability across sites indicates that the model is not able to give a robust quantitative biomass estimation. Indeed, the DMP algorithm does not take into account distinct efficiency factors in the conversion of light into biomass among different vegetation types. It should be reminded that, despite the three test sites featuring the same land cover and eco-region, the actual floristic composition and ecological characteristics could be much more different.

In Figure 9b are shown the effect of the EF contribution (DMP^{JASO}*) over the three sites. The plots show a general increase in the capacity of the remote sensing estimation in each site to detect the variability of the field measurements if water stress is taken into account, as indicated by the increasing of regression coefficients. Moreover, in particular, the EF has reduced the overestimation of the model for poorly productive years, as shown by intercepts closer to zero.

Due to the observation of site-specific DMP product performance, in order to directly compare the two biomass estimations, satellite products and field data were normalized for each site. The normalized data allows one to remove the effect of local differences in the relation between satellite outputs and field biomass, visualizing only the overall model capability to detect the field data variance, rather than absolute values. Data were standardized and converted to z-scores by subtracting from each value the site average and then dividing the result by the standard deviation. In the analysis of time series, the z-score is a dimensionless quantity adopted to convert variables with different scales to a common domain [10,77].

In Figure 9c are shown the normalized data, both for DMP^{JASO} (gray dots) and DMP^{JASO}* (black dots). The data close to zero are near the population average, while data values below or above zero indicate

a positive or a negative anomaly, respectively. The top right and bottom left corners indicate that years were estimated, and the measured variables' data are in agreement.

The correlation coefficient of the normalized $DMP^{JASO}*$ ($r^2 = 0.73$, $p < 0.001$) indicates that there is a significative increase in the capacity of the remote sensing estimation to explain the variance of annual field biomass measurements if water stress (EF) is taken into account.

This result is in accordance with previous work [41], even if the analysis was conducted at a monthly time step using EF derived with MODIS data (LST and albedo), rather than with field-measured EF and MODIS EVI at an eight-day time step.

Finally, AIC was calculated in order to evaluate whether the increase in the input of the model compared to the basic DMP was compensated for by a significant increase in accuracy (a lower AIC value indicates a convenient model improvement) [69]. Despite the correction, proposed to increase the number of inputs in the biomass estimation, the usefulness of the EF approach ($DMP^{JASO}*$) is confirmed by the improved model performance, indicated by the higher correlations shown in Figure 9c and the lower AIC value (106) compared with the one obtained with DMP^{JASO} (112).

6. Conclusions

The work exploited an automatic procedure to calculate multitemporal evaporative fraction maps from low resolution albedo and land surface temperature satellite data over Niger and Chad. Up to now, this is the first time that multiyear (2000–2009), eight-day maps of the evaporative fraction were produced from low resolution satellite data and analyzed for the West African Sahel. The adopted methodology, based on previous scientific works and well suited for semi-arid areas, allowed producing maps able to identify patterns of wet and dry condition, which are coherent with the main ecological features related to land cover classes and precipitation regimes.

The satellite estimation of the evaporative fraction, despite the uncertainty related to the 1-km resolution of the data, resulted in being correlated with the measurements of evapotranspiration ($r^2 = 0.54$, $p < 0.001$) acquired for two years (2005–2006) by an eddy flux tower in Niger. The total variance of evapotranspiration is mainly explained by the measured net radiation (64%, $p < 0.001$), while the estimated evaporative fraction significantly improves the model with a further 6% of variance explanation ($p < 0.01$). These results demonstrate that the satellite-derived evaporative fraction is a reliable indicator of moisture, useful for savannah status monitoring.

We further tested the use of the evaporative fraction as a water availability indicator to improve the accuracy of an operational remote sensing product of biomass estimation based on the radiation use efficiency concept. When the satellite-derived evaporative fraction is used as an indicator of water stress in the model, the correlation between annual biomass ground measurements and satellite estimations, for 19 samples over three sites, significantly improves ($r^2 = 0.73$, $p < 0.001$) compared to the performance of the basic satellite product ($r^2 = 0.54$, $p < 0.001$). The appropriate water efficiency term derived from optical and thermal remote sensing data represents an advancement over previous studies conducted using only the evaporative fraction derived by *in situ* eddy covariance data.

These findings are encouraging for the monitoring of biomass over wide savannah areas using a satellite-based approach. Future studies are needed to better parameterize the radiation use efficiency

model and to calibrate existing products over different ecosystems, in order to take into account the limiting factors and efficiency in the conversion of light into biomass.

Acknowledgments

This research was partially supported by the Geoland-2 project (Contract No. 218795), which is a collaborative project (2008–2012) funded by the European Union under the seventh Framework Programme (http://www.gmes-geoland.info/) and by Space4Agri project in the framework agreement between Regione Lombardia and National Research Council (Convenzione Operativa No. 18091/RCC, 05/08/2013). We also acknowledge the three anonymous reviewers for the help provided in improving this manuscript.

Author Contributions

Conceived and designed the experiments: Mirco Boschetti, Francesco Nutini, Stefano Bocchi. Performed the experiments: Gabriele Candiani, Francesco Nutini. Analyzed the data: Francesco Nutini, Mirco Boschetti, Pietro Alessandro Brivio. Wrote the paper: Francesco Nutini, Mirco Boschetti, Gabriele Candiani, Pietro Alessandro Brivio.

Conflicts of Interest

The authors declare no conflict of interest.

References

1. Anyamba, A.; Tucker, C. Analysis of Sahelian vegetation dynamics using NOAA-AVHRR NDVI data from 1981–2003. *J. Arid Environ.* **2005**, *63*, 596–614.
2. Zorom, M.; Barbier, B.; Mertz, O.; Servat, E. Diversification and adaptation strategies to climate variability: A farm typology for the Sahel. *Agric. Syst.* **2013**, *116*, 7–15.
3. Soler, C.M.T.; Maman, N.; Zhang, X.; Mason, S.C.; Hoogenboom, G. Determining optimum planting dates for pearl millet for two contrasting environments using a modelling approach. *J. Agric. Sci.* **2008**, *146*, 445–459.
4. Mortimore, M.J.; Adams, W.M. Farmer adaptation, change and "crisis" in the Sahel. *Glob. Environ. Chang.* **2001**, *11*, 49–57.
5. FAO. Available online: www.fao.org/emergencies/crisis/sahel/en (accessed on 14 April 2014).
6. Mertz, O.; Mbow, C.; Maiga, A.; Diallo, D.; Reenberg, A.; Diouf, A.; Barbier, B.; Moussa, I.B.; Zorom, M.; Ouattara, I.; *et al.* Climate factors play a limited role for past adaptation strategies in West Africa. *Ecol. Soc.* **2010**, *15*. Available on line: http://www.ecologyandsociety.org/vol15/iss4/art25/ (accessed on 14 April 2014).
7. Wang, J.; Li, X.; Lu, L.; Fang, F. Estimating near future regional corn yields by integrating multi-source observations into a crop growth model. *Eur. J. Agron.* **2013**, *49*, 126–140.
8. Tucker, C.J.; Vanpraet, C.L.; Sharman, M.J.; van Ittersum, G. Satellite remote sensing of total herbaceous biomass production in the senegalese sahel: 1980–1984. *Remote Sens. Environ.* **1985**, *17*, 233–249.

9. Hein, L.; de Ridder, N.; Hiernaux, P.; Leemans, R.; de Wit, A.; Schaepman, M. Desertification in the Sahel: Towards better accounting for ecosystem dynamics in the interpretation of remote sensing images. *J. Arid Environ.* **2011**, *75*, 1164–1172.
10. Boschetti, M.; Nutini, F.; Brivio, P.A.; Bartholomé, E.; Stroppiana, D.; Hoscilo, A. Identification of environmental anomaly hot spots in West Africa from time series of NDVI and rainfall. *ISPRS J. Photogramm. Remote Sens.* **2013**, *78*, 26–40.
11. Olsson, L.; Eklundh, L.; Ardo, J. A recent greening of the Sahel—Trends, patterns and potential causes. *J. Arid Environ.* **2005**, *63*, 556–566.
12. Seaquist, J.; Hickler, T.; Eklundh, L. Disentangling the effects of climate and people on Sahel vegetation dynamics. *Biogeosciences* **2009**, *6*, 469–477.
13. Herrmann, S.; Anyamba, A.; Tucker, C. Recent trends in vegetation dynamics in the African Sahel and their relationship to climate. *Glob. Environ. Chang.* **2005**, *15*, 394–404.
14. Huber, S.; Fensholt, R.; Rasmussen, K. Water availability as the driver of vegetation dynamics in the African Sahel from 1982 to 2007. *Glob. Planet. Chang.* **2011**, *76*, 186–195.
15. Fensholt, R.; Rasmussen, K. Analysis of trends in the Sahelian "rain-use efficiency" using GIMMS NDVI, RFE and GPCP rainfall data. *Remote Sens. Environ.* **2011**, *115*, 438–451.
16. Sandholt, I.; Rasmussen, K.; Andersen, J. A simple interpretation of the surface temperature/vegetation index space for assessment of surface moisture status. *Remote Sens. Environ.* **2002**, *79*, 213–224.
17. Bastiaanssen, W.G.M.; Menenti, M.; Feddes, R.A.; Holtslag, A.A.M. A remote sensing surface energy balance algorithm for land (SEBAL). 1. Formulation. *J. Hydrol.* **1998**, *212–213*, 198–212.
18. Verstraeten, W.W.; Veroustraete, F.; Feyen, J. Estimating evapotranspiration of European forests from NOAA-imagery at satellite overpass time: Towards an operational processing chain for integrated optical and thermal sensor data products. *Remote Sens. Environ.* **2005**, *96*, 256–276.
19. Allen, R.; Tasumi, M.; Trezza, R. Satellite-based energy balance for mapping evapotranspiration with internalized calibration (METRIC)—Model. *J. Irrig. Drain. Eng.* **2007**, 380–394.
20. Irmak, A.; Ratcliffe, I.; Hubbard, K. Estimation of land surface evapotranspiration with a satellite remote sensing procedure. *Gt. Plains Res.* **2011**, *21*, 73–88.
21. Li, X.; Lu, L.; Yang, W.; Cheng, G. Estimation of evapotranspiration in an arid region by remote sensing—A case study in the middle reaches of the Heihe River Basin. *Int. J. Appl. Earth Obs. Geoinf.* **2012**, *17*, 85–93.
22. Sun, Z.; Gebremichael, M.; Ardö, J.; Nickless, A.; Caquet, B.; Merboldh, L.; Kutschi, W. Estimation of daily evapotranspiration over Africa using MODIS/Terra and SEVIRI/MSG data. *Atmos. Res.* **2012**, *112*, 35–44.
23. Hall, F.; Huemmrich, K. Satellite remote sensing of surface energy balance: Success, failures, and unresolved issues in FIFE. *J. Geophys. Res.* **1992**, *97*, 19061–19089.
24. Cragoa, R.; Brutsaert, W. Daytime evaporation and the self-preservation of the evaporative fraction and the Bowen ratio. *J. Hydrol.* **1996**, *178*, 241–255.
25. Crago, R.D. Conservation and variability of the evaporative fraction during the daytime. *J. Hydrol.* **1996**, *180*, 173–194.

26. Sobrino, J.A.; Gómez, M.; Jiménez-Muñoz, J.C.; Olioso, A. Application of a simple algorithm to estimate daily evapotranspiration from NOAA–AVHRR images for the Iberian Peninsula. *Remote Sens. Environ.* **2007**, *110*, 139–148.
27. Gomez, M.; Olioso, A.; Sobrino, J.; Jacob, F. Retrieval of evapotranspiration over the Alpilles/ReSeDA experimental site using airborne POLDER sensor and a thermal camera. *Remote Sens. Environ.* **2005**, *96*, 399–408.
28. Ciraolo, G.; Minacapilli, M.; Sciortino, M. Stima dell'evapotraspirazione effettiva mediante telerilevamento aereo iperspettrale. *J. Agric. Eng.* **2007**, *38*, 49–60.
29. Gentine, P.; Entekhabi, D.; Chehbouni, A.; Boulet, G.; Duchemin, B. Analysis of evaporative fraction diurnal behaviour. *Agric. For. Meteorol.* **2007**, *143*, 13–29.
30. Venturini, V.; Islam, S.; Rodriguez, L. Estimation of evaporative fraction and evapotranspiration from MODIS products using a complementary based model. *Remote Sens. Environ.* **2008**, *112*, 132–141.
31. Yang, D.; Chen, H.; Lei, H. Analysis of the diurnal pattern of evaporative fraction and its controlling factors over croplands in the Northern China. *J. Integr. Agric.* **2013**, *12*, 1316–1329.
32. Hoedjes, J.C.B.; Chehbouni, A.; Jacob, F.; Ezzahar, J.; Boulet, G. Deriving daily evapotranspiration from remotely sensed instantaneous evaporative fraction over olive orchard in semi-arid Morocco. *J. Hydrol.* **2008**, *354*, 53–64.
33. Bastiaanssen, W.G.M.; Ali, S. A new crop yield forecasting model based on satellite measurements applied across the Indus Basin, Pakistan. *Agric. Ecosyst. Environ.* **2003**, *94*, 321–340.
34. Bastiaanssen, W.G.M.; Pelgrum, H.; Droogers, P.; de Bruin, H.A.R.; Menenti, M. Area-average estimates of evaporation, wetness indicators and top soil moisture during two golden days in EFEDA. *Agric. For. Meteorol.* **1997**, *87*, 119–137.
35. Kustas, W.; Schmugge, T.; Humes, K.; Jackson, T.; Parry, R.; Weltz, M.; Moran, M. Relationships between evaporative fraction and remotely sensed vegetation index and microwave brightness temperature for semiarid rangelands. *J. Appl. Metereol.* **1993**, *32*, 1781–1790.
36. Kurc, S.A.; Small, E.E. Dynamics of evapotranspiration in semiarid grassland and shrubland ecosystems during the summer monsoon season, central New Mexico. *Water Resour. Res.* **2004**, *40*, doi:10.1029/2004WR003068.
37. Guyot, A.; Cohard, J.-M.; Anquetin, S.; Galle, S. Long-term observations of turbulent fluxes over heterogeneous vegetation using scintillometry and additional observations: A contribution to AMMA under Sudano-Sahelian climate. *Agric. For. Meteorol.* **2012**, *154–155*, 84–98.
38. Higuchi, A.; Kondoh, A.; Kishi, S. Relationship among the surface albedo, spectral reflectance of canopy, and evaporative fraction at grassland and paddy field. *Adv. Space Res.* **2000**, *26*, 1043–1046.
39. Yuan, W.; Liu, S.; Zhou, G.; Zhou, G.; Tieszen, L.L.; Baldocchi, D.; Bernhofer, C.; Gholz, H.; Goldstein, A.H.; Goulden, M.L.; *et al.* Deriving a light use efficiency model from eddy covariance flux data for predicting daily gross primary production across biomes. *Agric. For. Meteorol.* **2007**, *143*, 189–207.
40. Kanniah, K.D.; Beringer, J.; Hutley, L.B.; Tapper, N.J.; Zhu, X. Evaluation of Collections 4 and 5 of the MODIS Gross Primary Productivity product and algorithm improvement at a tropical savanna site in northern Australia. *Remote Sens. Environ.* **2009**, *113*, 1808–1822.

41. Sjöström, M.; Ardö, J.; Arneth, A.; Boulain, N.; Cappelaere, B.; Eklundh, L.; de Grandcourt, A.; Kutsch, W.L.; Merbold, L.; Nouvellon, Y. Exploring the potential of MODIS EVI for modeling gross primary production across African ecosystems. *Remote Sens. Environ.* **2011**, *115*, 1081–1089.
42. Jiang, L.; Islam, S. Estimation of surface evaporation map over southern Great Plains using remote sensing data. *Water Resour. Res.* **2001**, *37*, 329–340.
43. Roerink, G.; Su, Z.; Menenti, M. S-SEBI: A simple remote sensing algorithm to estimate the surface energy balance. *Phys. Chem. Earth Part B* **2000**, *25*, 147–157.
44. Galleguillos, M.; Jacob, F.; Prévot, L.; French, A.; Lagacherie, P. Comparison of two temperature differencing methods to estimate daily evapotranspiration over a Mediterranean vineyard watershed from ASTER data. *Remote Sens. Environ.* **2011**, *115*, 1326–1340.
45. Olivera-Guerra, L.; Mattar, C.; Galleguillos, M. Estimation of real evapotranspiration and its variation in Mediterranean landscapes of central-southern Chile. *Int. J. Appl. Earth Obs. Geoinf.* **2014**, *28*, 160–169.
46. Santos, C.A.C.; Bezerra, B.G.; Silva, B.B.; Rao, T.V.R. Assessment of daily actual evapotranspiration with SEBAL and S-SEBI algorithms in cotton crop. *Rev. Bras. Meteorol.* **2010**, *25*, 383–398.
47. Wang, K.; Dickinson, R. A review of global terrestrial evapotranspiration: Observation, modeling, climatology, and climatic variability. *Rev. Geophys.* **2012**, *50*, 1–54.
48. Ramankutty, N. Croplands in West Africa: A geographically explicit dataset for use in models. *Earth Interact.* **2004**, *8*, 1–22.
49. CRED Emergency Events Database. Available online: http://www.emdat.be/result-country-profile (accessed on 14 April 2014).
50. Brink, A.B.; Eva, H.D. Monitoring 25 years of land cover change dynamics in Africa: A sample based remote sensing approach. *Appl. Geogr.* **2009**, *29*, 501–512.
51. Arino, O.; Gross, D.; Ranera, F.; Leroy, M.; Bicheron, P.; Brockman, C.; Defourny, P.; Vancutsem, C.; Achard, F.; Durieux, L.; *et al.* GlobCover: ESA Service for Global Land Cover from MERIS. In Proceedings of the IEEE International Geoscience and Remote Sensing Symposium, IGARSS 2007, Barcelona, Spain, 23–28 July 2007; pp. 2412–2415.
52. USGS MODIS Data Products Table. Available online: https://lpdaac.usgs.gov/products/modis_products_table (accessed on 14 April 2014).
53. Smets, B.; Eerens, H.; Jacobs, T.; Royer, A. BioPar Dry Matter Productivity (DMP) Product User Manual. Available online: http://web.vgt.vito.be/documents/BioPar/g2-BP-RP-BP053-ProductUserManual-DMPV0-I1.00.pdf (accessed on 14 April 2014).
54. NOAA CPC The NOAA Climate Prediction Center African Rainfall Estimation Algorithm Version 2.0. Available online: http://www.cpc.ncep.noaa.gov/products/fews/RFE2.0_tech.pdf (accessed on 14 April 2014).
55. VITO Low & Medium Resolution EO-Products—Free Data. Available online: www.vito-eodata.be (accessed on 14 April 2014).
56. Justice, C.; Hiernaux, P. Monitoring the grasslands of the Sahel using NOAA AVHRR data: Niger 1983. *Int. J. Remote Sens.* **1986**, *7*, 37–41.

57. Bonifacio, R.; Dugdale, G.; Milford, J. Sahelian rangeland production in relation to rainfall estimates from Meteosat. *Int. J. Remote Sens.* **1993**, *14*, 2695–2711.
58. Mutanga, O.; Skidmore, A. Merging double sampling with remote sensing for a rapid estimation of fuelwood. *Geocarto Int.* **2004**, *19*, doi:10.1080/10106040408542327.
59. Ham, F.; Fillol, E. Pastoral Surveillance System and Feed Inventory in the Sahel. In *Conducting National Feed Assessments*; FAO: Rome, Italy, 2010; Volume 1998, pp. 83–114.
60. Oak Ridge National Laboratory Distributed Active Archive Center FLUXNET Web Page. Available online: http://fluxnet.ornl.gov (accessed on 14 April 2014).
61. Mauder, M.; Liebethal, C.; Göckede, M.; Leps, J.-P.; Beyrich, F.; Foken, T. Processing and quality control of flux data during LITFASS-2003. *Bound. Layer Meteorol.* **2006**, *121*, 67–88.
62. Ramier, D.; Boulain, N.; Cappelaere, B.; Timouk, F.; Rabanit, M.; Lloyd, C.R.; Boubkraoui, S.; Métayer, F.; Descroix, L.; Wawrzyniak, V. Towards an understanding of coupled physical and biological processes in the cultivated Sahel—1. Energy and water. *J. Hydrol.* **2009**, *375*, 204–216.
63. Sturges, H. The choice of a class interval. *J. Am. Stat. Assoc.* **1926**, *21*, 65–66.
64. De Castro Teixeira, A.H.; Bastiaanssen, W.G.M.; Ahmad, M.D.; Moura, M.S.B.; Bos, M.G. Analysis of energy fluxes and vegetation-atmosphere parameters in irrigated and natural ecosystems of semi-arid Brazil. *J. Hydrol.* **2008**, *362*, 110–127.
65. Fensholt, R.; Sandholt, I.; Rasmussen, M.S.; Stisen, S.; Diouf, A. Evaluation of satellite based primary production modelling in the semi-arid Sahel. *Remote Sens. Environ.* **2006**, *105*, 173–188.
66. Seaquist, J. A remote sensing-based primary production model for grassland biomes. *Ecol. Modell.* **2003**, *169*, 131–155.
67. Meroni, M.; Fasbender, D.; Kayitakire, F.; Pini, G.; Rembold, F.; Urbano, F.; Verstraete, M.M. Early detection of biomass production deficit hot-spots in semi-arid environment using FAPAR time series and a probabilistic approach. *Remote Sens. Environ.* **2014**, *142*, 57–68.
68. Loague, K.M.; Green, R.E. Statistical and graphical methods for evaluating solute transport models: Overview and application. *J. Contam. Hydrol.* **1991**, *7*, 51–73.
69. Akaike, H. A new look at the statistical model identification. *IEEE Trans. Autom. Control* **1974**, *19*, 716–723.
70. Bagayoko, F.; Yonkeu, S.; Elbers, J.; van de Giesen, N. Energy partitioning over the West African savanna: Multi-year evaporation and surface conductance measurements in Eastern Burkina Faso. *J. Hydrol.* **2007**, *334*, 545–559.
71. Son, N.T.; Chen, C.F.; Chen, C.R.; Chang, L.Y.; Minh, V.Q. Monitoring agricultural drought in the Lower Mekong Basin using MODIS NDVI and land surface temperature data. *Int. J. Appl. Earth Obs. Geoinf.* **2012**, *18*, 417–427.
72. Coakley, J. Reflectance and Albedo, Surface. Available online: http://curry.eas.gatech.edu/Courses/6140/ency/Chapter9/Ency_Atmos/Reflectance_Albedo_Surface.pdf (accessed on 14 April 2014).
73. ECOWAS-SWAC. The Ecologically Vulnerable Zone of Sahelian Countries. In *Atlas on Regional Integration in West Africa*; ECOWAS—SWAC/OECD: Abuja, Nigeria, 2006; pp. 2–12.
74. Leblanc, M.; Lemoalle, J.; Bader, J.; Tweed, S. Thermal remote sensing of water under flooded vegetation: New observations of inundation patterns for the Small'Lake Chad. *J. Hydrol.* **2011**, *404*, 87–98.

75. Nutini, F.; Boschetti, M.; Brivio, P.; Bocchi, S.; Antoninetti, M. Land-use and land-cover change detection in a semi-arid area of Niger using multi-temporal analysis of Landsat images. *Int. J. Remote Sens.* **2013**, *34*, 37–41.
76. Campbell, B.D.; Stafford Smith, D.M. A synthesis of recent global change research on pasture and rangeland production: Reduced uncertainties and their management implications. *Agric. Ecosyst. Environ.* **2000**, *82*, 39–55.
77. Barbosa, H.A.; Huete, A.R.; Baethgen, W.E. A 20-year study of NDVI variability over the Northeast Region of Brazil. *J. Arid Environ.* **2006**, *67*, 288–307.